

The THDMa revisited

Tania Robens^{1,*}

¹*Ruder Boskovic Institute, Bijenicka cesta 54, 10000 Zagreb, Croatia*

(Dated: December 15, 2021)

Abstract

The THDMa is a new physics model that extends the scalar sector of the Standard Model by an additional doublet as well as a pseudoscalar singlet and allows for mixing between all possible scalar states. In the gauge-eigenbasis, the additional pseudoscalar serves as a portal to the dark sector, with a priori any dark matter spins states. The option where dark matter is fermionic is currently one of the standard benchmarks for the experimental collaborations, and several searches at the LHC constrain the corresponding parameter space. However, most current studies constrain regions in parameter space by setting all but 2 of the 12 free parameters to fixed values.

In this work, we perform a generic scan on this model, allowing all parameters to float. We apply all current theoretical and experimental constraints, including bounds from current searches, recent results from B-physics, in particular $B_s \rightarrow X_s \gamma$, as well as bounds from astroparticle physics. We identify regions in the parameter space which are still allowed after these have been applied and which might be interesting for an investigation at current and future collider machines.

* trobens@irb.hr

I. INTRODUCTION

After the discovery of a scalar boson what complies with predictions of the Standard Model (SM) Higgs boson by the LHC experiments, the quest of additional particles that stem from possible further extensions of the SM scalar sector is an important task for the experimental collaborations. Furthermore, astroparticle observations give evidence for the existence of dark matter. In a standard cosmological description, the particle content of the SM alone does not suffice to explain these observations. Therefore, many beyond the SM (BSM) extensions in addition provide a dark matter candidate.

In this work, we concentrate on the model which has been proposed in [1–5]. It extends the scalar sector of the Standard Model by an additional doublet as well as a pseudoscalar singlet, which in turn couples to a fermionic dark matter candidate. The model therefore extends the scalar sector by 5 additional particles, which we label H, A, a, H^\pm in the mass eigenbasis, as well as a fermionic dark matter candidate χ . In the form discussed here, the model contains 14 free parameters after electroweak symmetry breaking, out of which 2 are fixed by the measurement of the 125 GeV scalar as well as electroweak precision measurements. Furthermore, the model's parameter space is subject to a large number of theoretical and experimental constraints, which we will discuss in detail below. Reference [6] contains a detailed discussion as well as benchmark recommendations for the LHC experimental collaborations; see also refs [7–15] for more recent work on this model. Finally, refs [16–34] report on experimental constraints from current collider searches on the parameter space in specific parameter regions¹. This manuscript is organized as follows. In section II, we briefly review the setup of the model, including the introduction of conventions used in this work. In section III, we discuss current theoretical and experimental bounds that need to be imposed. Section IV introduces the setup of our scan and identifies regions in parameter space that are still allowed after all constraints are taken into account. We present a first glance at possible processes at e^+e^- colliders in section V, and conclude in section VI.

II. THE MODEL

The model discussed in this work has been introduced in references [1–5], and we refer the reader to these works for a detailed discussion of the model setup. We here just list generic features for brevity. We largely follow the nomenclature of [6].

The field content of the THDMa in the gauge eigenbasis consists of two scalar fields $H_{1,2}$ which transform as doublets under the $SU(2) \times U(1)$ gauge group, and additional pseudoscalar P transforming as a singlet, as well as a dark matter candidate χ which we choose to be fermionic. The two Higgs Doublet Model (THDM) part of the potential is

¹ Projections for the HL-LHC sensitivity can be found in [35–38].

given by

$$V_{\text{THDM}} = \mu_1 H_1^\dagger H_1 + \mu_2 H_2^\dagger H_2 + \lambda_1 (H_1^\dagger H_1)^2 + \lambda_2 (H_2^\dagger H_2)^2 + \lambda_3 (H_1^\dagger H_1)(H_2^\dagger H_2) \quad (1)$$

$$+ \lambda_4 (H_1^\dagger H_2)(H_2^\dagger H_1) + \left[\mu_3 H_1^\dagger H_2 + \lambda_5 (H_1^\dagger H_2)^2 + h.c. \right] \quad (2)$$

Fields are decomposed according to (see also e.g. [39])

$$H_i = \begin{pmatrix} \phi_i \\ \frac{1}{\sqrt{2}}(v_i + \rho_i + i\eta_i) \end{pmatrix} \quad (3)$$

where

$$v_1 = v \cos \beta, \quad v_2 = v \sin \beta. \quad (4)$$

The scalar potential is

$$V_P = \frac{1}{2} m_P^2 P^2 + \lambda_{P1} H_1^\dagger H_1 P^2 + \lambda_{P2} H_2^\dagger H_2 P^2 + (ib_P H_1^\dagger H_2 P + h.c.). \quad (5)$$

Finally, the coupling between the visible and the dark sector is mediated via the interaction

$$\mathcal{L}_\chi = -i y_\chi P \bar{\chi} \gamma_5 \chi.$$

Couplings of the scalar sector to the fermionic sector are equivalent to a THDM type II (see e.g. [39]) and follow from

$$\mathcal{L}_Y = - \sum_{i=1,2} \left\{ \bar{Q} Y_u^i \tilde{H}_i u_R + \bar{Q} Y_d^i H_i d_R + \bar{L} Y_\ell^i H_i \ell_R + h.c. \right\},$$

where $Y_{u,d}^i$ denote the Yukawa matrices, Q and L are left-handed quark and lepton doublets, u_R , d_R , ℓ_R label right-handed up-type, down-type, and leptonic singlets, and $\tilde{H} = \epsilon H_i^*$, where $\epsilon = i\sigma_2$ denotes the two-dimensional antisymmetric tensor. We impose an additional Z_2 symmetry on the model, under which the doublets transform as $H_1 \rightarrow H_1$, $H_2 \rightarrow -H_2$, in order to avoid contributions from flavour changing neutral currents. We furthermore set the transformation properties of the additional fields as $P \rightarrow P$, $\chi \rightarrow -\chi$. In this work, we concentrate on the case where $Y_1^u = Y_2^d = Y_2^\ell = 0$, which corresponds to a type II classification of Yukawa couplings in the THDM notation and can be achieved by requiring $u_R \rightarrow -u_R$ under the said symmetry. Note the terms $\sim \mu_3$, b_P induce a soft Z_2 breaking.

After electroweak symmetry breaking, the model is characterized by in total 14 free parameters. The above potential induces standard mixing for the THDM part of the potential, which we characterize by $\cos(\beta - \alpha)$, $\tan \beta$ using standard notation. Furthermore, V_P introduces a mixing between the pseudoscalar part of the THDM and the new pseudoscalar P , with physical states given by

$$\begin{pmatrix} a \\ A \end{pmatrix} = \begin{pmatrix} c_\theta & -s_\theta \\ s_\theta & c_\theta \end{pmatrix} \begin{pmatrix} P \\ A^0 \end{pmatrix}$$

where we use the notation $c_x \equiv \cos x$, $s_x \equiv \sin x$ here and in the following and A^0 denotes the mass-eigenstate of the pseudoscalar from V_{THDM} prior to mixing. We choose as free parameters

$$v, m_h, m_A, m_H, m_{H^\pm}, m_a, m_\chi, \cos(\beta - \alpha), \tan\beta, \sin\theta, y_\chi, \lambda_3, \lambda_{P_1}, \lambda_{P_2} \quad (6)$$

following the suggestions in [6]. Relations between these and other quantities in the Lagrangian can be found in appendix A.

For the parameters in eqn (6), v and m_h are fixed to be ~ 246 GeV and ~ 125 GeV, respectively². We are therefore left with 12 parameters which can a priori vary, but are obviously subject to theoretical and experimental constraints. Previous studies of this model usually chose to consider scenarios where all but a few are fixed, in order to facilitate the phenomenological exploration and to provide consistent benchmark scenarios for comparison. In this work, we allow all parameters to float and determine regions in the models parameter space that are highly populated³.

III. THEORETICAL AND EXPERIMENTAL CONSTRAINTS

The models parameter space is subject to a list of theoretical and experimental constraints, which we list below.

A. Perturbativity, perturbative unitarity and positivity of the potential

In order to guarantee positivity of the potential, several relations between the potential parameters need to be obeyed (see e.g. [6, 12, 14]). In the notation introduced here, they are given by

$$\lambda_{1,2,P_1,P_2} \geq 0, \lambda_3 \geq -2\sqrt{\lambda_1\lambda_2}, \lambda_3 + \lambda_4 - 2|\lambda_5| \geq -2\sqrt{\lambda_1\lambda_2}.$$

Furthermore, we require the self-couplings in the potential to obey an upper limit, which we chose as 4π . We therefore have

$$|\lambda_i| \leq 4\pi, \left| \frac{b_P}{v} \right| \leq 4\pi.$$

Finally, bounds from perturbative unitarity are implemented using the perturbative unitarity bounds derived in [12]; we refer the reader to that work for more details as well as explicit analytic expressions. We furthermore check that eqn (3.11) of [14] (taken from [3]) is fulfilled.

² In principle one can also consider the case that $m_H \sim 125$ GeV, with m_h being a lighter resonance. We discard this scenario in the following.

³ Fine-tuned regions might exist within this model which are missed in a generic scan setup.

B. Constraints from electroweak precision observables, flavour constraints, and total widths

These bounds are tested via an implementation in SPheno [40, 41], using an interface to Sarah [42–46]. Constraints from measurements of electroweak precision observables are taken into account using the oblique parameters S, T, U [47–49] as a parametrization. We take the latest fit results from the Gfitter collaboration [50–52], with central values given by

$$S = 0.04 \pm 0.11, T = 0.09 \pm 0.14, U = -0.02 \pm 0.11$$

and the correlation matrix as given in the above references. We demand $\Delta\chi^2 \leq 8.02489$, which corresponds to a 2σ region around the central value determined by the SM decoupling.

Two Higgs doublet models and their extensions are also subject to strong bounds from flavour constraints, cf. e.g. [52, 53]. Especially the $m_{H^\pm}, \tan\beta$ plane is strongly constrained by precision flavour observables as e.g. $B \rightarrow X_s \gamma$, $B_s \rightarrow \mu^+ \mu^-$, and ΔM_s . For these variables, we consider the following allowed regions:

- $B \rightarrow X_s \gamma$

The most recent results on the theoretical calculation of this variable, including higher order calculations up to NNLO in QCD, have been presented in [54], superseding previous results [55]. In particular, the charged scalar mass is pushed to even higher masses. We implement the lower bound in this variable using a two-dimensional fit function [56] that reflects the bounds derived in [54].

- $B_s \rightarrow \mu^+ \mu^-$

The ATLAS, CMS and LHCb combination using 2011-2016 LHC data for the branching ratio $B_s \rightarrow \mu^+ \mu^-$ is given by [57]

$$(B_s \rightarrow \mu^+ \mu^-)^{\text{comb}} = [2.69^{+0.37}_{-0.35}] \times 10^{-9}. \quad (7)$$

In principle, theoretical predictions depend on all novel scalar masses (see e.g. [58]).

In the decoupling limit, SPheno renders the SM output

$$B_s \rightarrow \mu^+ \mu^- = 2.96 \times 10^{-9},$$

while the most recent theoretical calculation yields [59]

$$B_s \rightarrow \mu^+ \mu^- = (3.66 \pm 0.14) \times 10^{-9}.$$

Note that this disagrees with the experimental result (eqn. (7)) by 2.5σ .

In order to account for the missing higher order corrections, we apply a multiplicative correction factor to the Spheno result.

Assuming again a similar error in the theory calculation, and taking into account the additional higher order shift to the Spheno result, we then have

$$(B_s \rightarrow \mu^+ \mu^-)^{\text{Spheno}} \in [1.26; 3.14] \times 10^{-9},$$

where we allow for a 3σ deviation.

- ΔM_s

The most recent experimental result for this value is given by $\Delta M_s (\text{ps}^{-1}) = 17.757 \pm 0.020 \pm 0.007$ [60].

We use the following derivation for the SM prediction for this value: We start with eqn. (31) of [61]

$$\Delta M_s = 17.24 \text{ps}^{-1} \left(\frac{|V_{tb} V_{ts}^*|}{0.04} \right)^2 \frac{S(\overline{m}_t^2/m_W^2)}{2.35} \frac{f_{B_s}^2 \mathcal{B}_{B_s}}{(0.21 \text{GeV})^2} |\Delta_s|$$

which shows the dependency of this variable on external, experimentally determined parameters. The above expression was updated to [62, 63]

$$\Delta M_s = 17.3 \text{ps}^{-1} \frac{f_{B_s}^2 \mathcal{B}_{B_s}}{(211.84 \text{MeV})^2} \frac{|V_{cb}|^2}{0.04089^2}.$$

For input values [64–67]

$$f_{B_s} = (230.3 \pm 1.3) \text{MeV}, \hat{\mathcal{B}}_{B_s} = 1.232 \pm 0.053, V_{cb} = (42.2 \pm 0.8) \times 10^{-3},$$

together with the conversion factor $\hat{\mathcal{B}}_{B_s} = 1.52319 \mathcal{B}_{B_s}$ [62], we then obtain

$$\Delta M_s = (17.61 \pm 1.05) \text{ps}^{-1},$$

where we furthermore assumed an intrinsic error of 0.2 on the central value [63], which mainly stems from uncertainties of the top mass⁴.

The Spheno decoupling result is given by $(\Delta M_s)^{\text{Spheno}} = 18.801 \text{ps}^{-1}$.

Assuming the new physics contributions to be multiplicative, while keeping the error additive⁵, we then have

$$[\Delta M_s (\text{ps}^{-1})]^{\text{Spheno}} \in [16.71; 21.19] \text{ps}^{-1} \quad (8)$$

as an allowed 2σ range for this value.

⁴ Neglecting this leads to a slightly smaller error of $\pm 1.03 \text{ps}^{-1}$.

⁵ TR wants to thank M. Mikolaj for useful discussions regarding this point.

Finally, although not strictly required, we impose an upper bound on the width over mass ratio on all new scalars. For the 125 GeV candidate, we require that [68]

$$\Gamma_{h,125} \leq 9 \text{ MeV}. \quad (9)$$

For all other scalars, we impose

$$\Gamma/M \leq 0.5. \quad (10)$$

We consider this a very lenient bound in order to allow a detailed investigation of the parameter space; in practise, ratios larger than 10 – 20% already strongly question the applicability of perturbative treatment for such states.

C. Collider bounds

Agreement with current measurements of the 125 GeV signal strength as well as agreement with null-results from a large number of searches have been tested by interfacing the model with HiggsBounds [69–75] and HiggsSignals [74, 76–79]. Furthermore, the model is additionally constrained by dedicated searches by the LHC experiments; we have implemented the corresponding bounds in a pseudo-approximate approach and leave a detailed recast analysis for future work. All production cross sections have been produced using Madgraph5 [80], with the UFO model provided in [4, 81].

• Bounds from $\ell^+\ell^- + \text{MET}$ searches

We consider the experimental bounds presented in [22], which corresponds to a CMS search for this channel mediated via Za production using full Run 2 luminosity. For the parameters specified in figure 8 in that work, we generate parton-level events. In order to marginally mimick the experimental cuts, we have imposed

$$p_{\perp,\ell} > 25 \text{ GeV}, \cancel{E}_{\perp} > 80 \text{ GeV}, m_{\ell\ell} \in [76, 106] \text{ GeV}, \\ p_{\perp}^{\ell\ell} > 60 \text{ GeV}, |\eta_{\ell}| \leq 2.4, \Delta R_{\ell\ell} \leq 1.8$$

at parton-level. Results for two specific parameter points using the above cuts are given in table I.

A first estimate for sensitivity regions would therefore be to only allow parameter points with

$$\sigma \leq 0.0007314 \text{ pb}, \quad (11)$$

and simulating all parameter points using the cuts specified above. However, this is especially computationally intensive. Therefore, it is useful to consider the main channel leading to the above signature, which is

$$pp \rightarrow H \rightarrow aZ$$

m_a	m_A	$\sin \theta$	$\tan \beta$	$\sigma[\text{pb}]$
220 GeV	400 GeV	0.35	1	0.01066(3)
320 GeV	650 GeV	0.35	1	0.00332(3)
420 GeV	1000 GeV	0.35	1	0.0007296(9)

TABLE I. Results for parton-level generation with rudimentary cuts for points which are excluded by $\ell^+ \ell^- + \cancel{E}_\perp$ searches in [22]. Other values are set to $m_H = m_{H^\pm} = m_A$, $m_\chi = 10 \text{ GeV}$, $\cos(\beta - \alpha) = 0$, $\lambda_3 = \lambda_{P_1} = \lambda_{P_2} = 3$, $y_\chi = 1$.

m_a	m_A	m_H	$\sigma_H [\text{pb}]$	$H \rightarrow a Z$	$a \rightarrow \chi \bar{\chi}$	$\sigma_{Z\chi\bar{\chi}}^{\text{fac}} [\text{pb}]$
220 GeV	400 GeV	400 GeV	3.70(1)	0.11	1	0.407(1)
320 GeV	650 GeV	650 GeV	0.534(1)	0.13	1	0.0694(1)
420 GeV	1000 GeV	1000 GeV	0.0497(2)	0.28	0.86	0.01197(5)

TABLE II. Parameter points in table I, relevant quantities. Last column is derived from previous entries.

with subsequent decays $a \rightarrow \chi \bar{\chi}$, $Z \rightarrow \ell^+ \ell^-$. The value from factorized onshell production times decay branching ratios into the $Z \chi \bar{\chi}$ final state for the above benchmark points is given in table II.

We therefore could use as a naive condition that

$$\sigma_{Z\chi\bar{\chi}}^{\text{fac}} \equiv \sigma_{pp \rightarrow H} \times \text{BR}_{H \rightarrow Z a} \times \text{BR}_{a \rightarrow \chi \bar{\chi}} \leq 0.01207. \quad (12)$$

A more thorough inspection shows that the above bound has to be modified to

$$\sigma_{Z\chi\bar{\chi}}^{\text{fac}} \leq 0.009085 \text{ pb}$$

in order to capture all points from our scan which obey eqn (11).

• Bounds from $h + \text{MET}$ searches

The above channel for this model has been investigated in [31, 32] by the ATLAS collaboration using the full Run 2 dataset. We found that results for the $b\bar{b}$ decay of the h [32] supersede those of the $\gamma\gamma$ decay [31], and therefore concentrate on the former in the following. Note that the search has been separated into a resolved and an unresolved region; for the resolved, we require $\cancel{E}_\perp > 500 \text{ GeV}$, while for the unresolved we have $\cancel{E}_\perp \in [150; 500] \text{ GeV}$, $p_{\perp, h} > 100 \text{ GeV}$. We show the values using these cuts for some sample points in table III.

m_a	m_A	$\sigma_{\text{res}}[\text{pb}]$	$\sigma_{\text{unres}}[\text{pb}]$
640 GeV	1350 GeV	0.001898 (2)	0.0003709 (5)
300 GeV	500 GeV	0.00493 (2)	$6.79(1) \times 10^{-7}$
180 GeV	1800 GeV	0.00994 (8)	0.0005817 (2)

TABLE III. Results for parton-level generation with rudimentary cuts for points which are excluded by $h+\cancel{E}_\perp$ searches in [32]. Other values are set to $m_H = m_{H^\pm} = m_A$, $m_\chi = 10 \text{ GeV}$, $\cos(\beta-\alpha) = 0$, $\lambda_3 = \lambda_{P_1} = \lambda_{P_2} = 3$, $y_\chi = 1$, $\sin\theta = 0.35$, $\tan\beta = 1$. $\sigma_{\text{res/unres}}$ refer to the resolved/unresolved region as discussed in the text.

m_a	m_A	$\sigma_{\text{res}}[\text{pb}]$	$\sigma_{\text{unres}}[\text{pb}]$
500 GeV	1200 GeV	0.00466 (1)	0.000357 (1)
180 GeV	1550 GeV	0.002816 (1)	0.001366 (2)
300 GeV	500 GeV	0.00493 (2)	$6.79(1) \times 10^{-7}$

TABLE IV. Results for parton-level generation with rudimentary cuts for points which are excluded by $h+\cancel{E}_\perp$ searches in [32]. Other values are set to $m_H = m_{H^\pm} = m_A$, $m_\chi = 10 \text{ GeV}$, $\cos(\beta-\alpha) = 0$, $\lambda_3 = \lambda_{P_1} = \lambda_{P_2} = 3$, $y_\chi = 1$, $\sin\theta = 0.35$, $\tan\beta = 1$. $\sigma_{\text{res/unres}}$ refer to the resolved/unresolved region as discussed in the text.

A priori, the dominant production times decay stems from

$$pp \rightarrow A \rightarrow h a \rightarrow h \chi \bar{\chi}, \quad (13)$$

where additional contributions can come from

$$pp \rightarrow A(a) \rightarrow h A(a) \rightarrow h \chi \bar{\chi}, \quad (14)$$

i.e., non-resonant production of $A(a)$ and subsequent decays.

From table IV, we see that we can roughly exclude points for which the conditions

$$\sigma_{h+\cancel{E}_\perp, \text{res}} \leq 0.002818 \text{ pb}, \quad \sigma_{h+\cancel{E}_\perp, \text{unres}} \leq 6.81 \times 10^{-7} \text{ pb} \quad (15)$$

are not fulfilled⁶.

For the two points giving the bounds in eqn (15), we have in a factorized approach

$$\begin{aligned} \sigma_{180,1550}^{\text{fac}} &= \sigma_A \times \text{BR}_{A \rightarrow h a} \times \text{BR}_{a \rightarrow \chi \bar{\chi}} = 0.001728(2) \text{ pb}, \\ \sigma_{300,500}^{\text{fac}} &= \sigma_A \times \text{BR}_{A \rightarrow h a} \times \text{BR}_{a \rightarrow \chi \bar{\chi}} = 0.1158(1) \text{ pb}. \end{aligned}$$

A more detailed investigation show that for the first parameter point, (13) provides around 62% of the cross-section in the resolved region, while for the second, the processes in (14) mainly contribute. In the following, we require that

⁶ We again want to emphasize that this only corresponds to a very rough sensitivity estimate. In particular, different regions of the parameter space can be more sensitive to the resolved/unresolved region.

$$\sigma_{\text{fac}} = \sigma_A \times \text{BR}_{A \rightarrow ah} \times \text{BR}_{a \chi \bar{\chi}} \leq 0.001732 \text{ pb.}$$

For our sample points, we have explicitly checked that this value cuts out all parts of parameter space where $\sigma_{h+\cancel{E}_\perp} \geq 0.002818 \text{ pb.}$

- **Bounds from $H^+ \bar{t}b$, $H^+ \rightarrow t \bar{b}$ searches**

Searches for the THDM sector of the model can be constrained by the above process, which has been presented e.g. by the ATLAS collaboration [25] using an integrated luminosity of 139 fb^{-1} , which we compare to the upper bound on the cross section as available from Hepdata [82]. Even a comparison with the production cross section for the process

$$pp \rightarrow H^+ \bar{t}b$$

prior to the charged scalars decay shows that this search is not yet sensitive in the parameter space investigated here. This is mainly caused by the lower limit on $\tan \beta$ from $B \rightarrow X_s \gamma$ which preselects point with higher $\tan \beta$ values.

- **Bounds from $Wt + \text{MET}$ searches**

The ATLAS collaboration has presented results for this model in the above channel using full Run2 data [23]. They give results for bounds derived from single and double top production, divided into several search regions. We here implemented their results into grid-like upper bounds on the total production cross section from single-top like processes, with values taken from figure 28 of the auxiliary material available from [83]. In the mass region considered here, the smallest upper bound is around 32 fb^7 .

- **Bounds from $t\bar{t}/b\bar{b} + \text{MET}$ final states**

The $t\bar{t}$ final states have been investigated in [26, 28] using full Run 2 data. We note that the simulation for the signal a different model file was used, and cross sections were rescaled to NLO predictions [84]. In the comparison here, we stick to leading order, as QCD higher order corrections are universal for both models, differing only in the electroweak sector, as long a dominant production is assumed via an s-channel mediator. In table V, we give our predictions for the theory cross section predictions shown in figure 15 of that reference. Note that for generation we used $\sin \theta = 1/\sqrt{2}$, as otherwise no significant coupling to both the SM and the dark sector can be achieved. The values in table V have been rescaled accordingly⁸. We use $\cancel{E}_\perp > 230 \text{ GeV}$.

⁷ Note that including $t\bar{t}$ results will improve these bounds. However, here theoretical cross sections which were e.g. used in figure 31 of the above auxiliary material includes detector simulation and cuts; we thank the authors of the above reference for useful discussions regarding this point. Including these would require a recast-type investigation, which is beyond the scope of the current work.

⁸ The coupling of a to $t\bar{t}$ is rescaled by $\sin \theta$, while the coupling to $\chi \bar{\chi}$ is rescaled by $\cos \theta$. We therefore, in comparison to the calculating in [26] for $g = 1$ obtain an additional factor $\frac{1}{4}$ in the results.

m_a [GeV]	σ [pb]	fac	σ^{excl} [pb]
60	0.0570 (2)	0.45	0.02565 (9)
100	0.0521 (3)	0.5	0.0261 (2)
200	0.0371 (2)	0.8	0.0297 (2)
300	0.0241 (1)	1.02	0.0246 (1)
400	0.00868 (4)	4	0.0347 (2)

TABLE V. Results for parton-level generation with rudimentary cuts for points which are excluded by $t\bar{t} + \cancel{E}_\perp$ searches in [26] via a mediation. Other values are set to $m_H = m_A = m_{H^\pm} = 600$ GeV, $m_\chi = 1$ GeV, $\cos(\beta - \alpha) = 0$, $\lambda_3 = \lambda_{P_1} = \lambda_{P_2} = 3$, $y_\chi = 1$, $\tan\beta = 1$. The factor corresponds to a rough estimate of the multiplicative factor from figure 15 of that reference. The last column gives the actual exclusion cross section.

m_a [GeV]	σ [pb]	fac	σ^{excl} [pb]
60	0.2028 (8)	0.24	0.0487 (2)
100	0.1716 (8)	0.25	0.0429 (2)
200	0.1016 (4)	0.5	0.0508 (2)
300	0.0576 (3)	0.8	0.0461 (2)
400	0.01900 (8)	1.4	0.0266 (1)

TABLE VI. Results for parton-level generation with rudimentary cuts for points which are excluded by $t\bar{t} + \cancel{E}_\perp$ searches in [28] via a mediation. Other values are set to $m_H = m_A = m_{H^\pm} = 600$ GeV, $m_\chi = 1$ GeV, $\cos(\beta - \alpha) = 0$, $\lambda_3 = \lambda_{P_1} = \lambda_{P_2} = 3$, $y_\chi = 1$, $\tan\beta = 1$. The factor corresponds to a rough estimate of the multiplicative factor from figure 15 of that reference. The last column gives the actual exclusion cross section.

Following the same logic as before, we see that we can naively exclude points where

$$t\bar{t} + \cancel{E}_\perp : \sigma \leq 0.0248 \text{ pb}$$

For the search in [28], we use $\cancel{E}_\perp \gtrsim 110$ GeV. Cross-sections were calculated as above, and the respective values are given in table VI.

This leads to

$$t\bar{t} + \cancel{E}_\perp : \sigma \leq 0.0268 \text{ pb}$$

for this \cancel{E}_\perp cut.

The $b\bar{b}$ final state has been investigated in [27] using full Run 2 data. As before, we here use the model file we used in the whole paper, which corresponds to a UV-complete model, at leading-order. Again the mixing angle has been set to $\sin\theta = 1/\sqrt{2}$. Values are shown in table VII. We use $\cancel{E}_\perp \geq 180$ GeV, $|p_{\perp,b}| \geq 50$ GeV for the numbers in that table.

m_a [GeV]	σ [pb]	fac	σ^{excl} [pb]
60	0.000860 (4)	20	0.01720 (8)
100	0.000730 (4)	30	0.0219 (1)
200	0.000422 (2)	100	0.0422 (2)
300	0.0002336 (8)	140	0.0327 (1)
500	0.00003536 (8)	400	0.01414 (3)

TABLE VII. Results for parton-level generation with rudimentary cuts for points which are excluded by $b\bar{b} + \cancel{E}_\perp$ searches in [27] via a mediation. Other values are set to $m_H = m_A = m_{H^\pm} = 600$ GeV, $m_\chi = 1$ GeV, $\cos(\beta - \alpha) = 0$, $\lambda_3 = \lambda_{P_1} = \lambda_{P_2} = 3$, $y_\chi = 1$, $\tan\beta = 1$. The factor corresponds to a rough estimate of the multiplicative factor from figure 10 of that reference. The last column gives the actual exclusion cross section.

This leads to

$$b\bar{b} + \cancel{E}_\perp : \sigma \leq 0.01420 \text{ pb}$$

The same channels have been investigated in [16] using an integrated luminosity of 36 fb^{-1} . In tables VIII and IX, we again show the production cross section for selected points from that reference, as well as resulting upper bounds on these cross sections. For $t\bar{t} + \cancel{E}_\perp$, we use $\cancel{E}_\perp \gtrsim 300$ GeV; for $b\bar{b} + \cancel{E}_\perp$, we take $\cancel{E}_\perp \gtrsim 180$ GeV, $p_{\perp,b} \gtrsim 20$ GeV. As in the comparison with results from [26], we used a slightly different way to generate the event samples for consistency reasons.

Following the same logic as before, we now require that

$$\sigma_{t\bar{t}+\cancel{E}_\perp} \leq 0.000703 \text{ pb}; \sigma_{b\bar{b}+\cancel{E}_\perp} \leq 0.578 \text{ pb}$$

with the cuts as specified above⁹.

• Bounds from monojet searches

We also compare to the results for monojet searches as presented in [86]. As discussed above, this work uses a different model file, which we accommodated for by setting $\sin\theta = \frac{1}{\sqrt{2}}$ and rescaling our result accordingly. Bounds on the signal strength are taken from HEPdata [87]. Our results are presented in table X. We applied a cut on the missing transverse energy $\cancel{E}_\perp \gtrsim 250$ GeV.

The table translates to a maximal allowed cross section of around $\sigma_{\text{lim}} = 0.0638 \text{ pb}$.

⁹ Note different cuts apply. Also, in [27], results for $m_a < m_\chi$ were not presented. These lead to quite strong constraints in the analysis in [16].

m_a	m_χ	$\sigma[\text{pb}]$	fac	$\sigma^{\text{excl}}[\text{pb}]$
70 GeV	1 GeV	0.02536 (8)	1.37	0.0347 (1)
100 GeV	1 GeV	0.02392 (1)	1.41	0.03373 (1)
200 GeV	1 GeV	0.01848 (8)	1.94	0.0359 (2)
300 GeV	1 GeV	0.01292 (8)	2.7	0.0349 (2)
500 GeV	1 GeV	0.00270 (2)	13.65	0.0369 (3)
10 GeV	30 GeV	0.000520 (4) (1)	44.56	0.0232 (2)
10 GeV	50 GeV	0.000368 (4)	63.25	0.0233 (3)
10 GeV	100 GeV	0.000170 (3)	166.52	0.023 (3)
10 GeV	200 GeV	0.000031(4)	736.94	0.0245 (3)
10 GeV	300 GeV	$2.92 (4) \times 10^{-7}$	2346.43	0.000685 (9)
10 GeV	500 GeV	$4.94 (4) \times 10^{-8}$	14628.82	0.000723 (5)

TABLE VIII. Results for parton-level generation with rudimentary cuts for points which are excluded by $t\bar{t} + \cancel{E}_\perp$ searches in [16]. Other values are set to $m_H = m_A = m_{H^\pm} = 600 \text{ GeV}$, $\cos(\beta - \alpha) = 0$, $\lambda_3 = \lambda_{P_1} = \lambda_{P_2} = 3$, $y_\chi = 1$, $\tan\beta = 1$. The factor has been taken from HEPData [85]. The last column gives the actual exclusion cross section.

m_a	$\sigma[\text{pb}]$	fac	$\sigma^{\text{excl}}[\text{pb}]$
70	0.001808 (8)	316.33	0.572 (3)
100	0.001584 (8)	400.243	0.634 (3)
200	0.001044 (4)	876.85	0.915 (4)
300	0.000479 (2)	1875.75	0.898 (4)
500	$6.83(4) \times 10^{-5}$	8581.11	0.586 (3)

TABLE IX. Results for parton-level generation with rudimentary cuts for points which are excluded by $b\bar{b} + \cancel{E}_\perp$ searches in [16]. Other values are set to $m_H = m_{H^\pm} = m_A = 600 \text{ GeV}$, $m_\chi = 1 \text{ GeV}$, $\cos(\beta - \alpha) = 0$, $\lambda_3 = \lambda_{P_1} = \lambda_{P_2} = 3$, $y_\chi = 1$, $\tan\beta = 1$. The factor has been taken from HEPData [85]. The last column gives the actual exclusion cross section.

D. Dark matter constraints

The THDMa renders a dark matter candidate and is therefore subject to constraints from astrophysical measurements, such as relic density and direct detection. We have made use of MadDM [88–90] for the calculation of relic density. For direct detection, we implemented the analytic expressions presented in [1]¹⁰. We compare these values to limits from the Planck collaboration [93], and require that

$$\Omega h^2 \leq 0.1224 \quad (16)$$

¹⁰ A more detailed analysis, as e.g. presented in [9, 12, 91, 92], is beyond the scope of the current work.

m_a	$\sigma[\text{pb}]$	fac	$\sigma^{\text{excl}}[\text{pb}]$
80	0.346(2)	0.78	0.270(2)
100	0.3352(4)	0.76	0.2547(3)
200	0.2812(4)	0.69	0.1940(3)
300	0.277(2)	0.51	0.141(1)
350	0.342(1)	0.36	0.123(4)
400	0.184(2)	0.56	0.1028(9)
450	0.1144(4)	0.87	0.0995(3)
500	0.0728(4)	1.2	0.0874(5)
600	0.0362(2)	2.4	0.0868(4)
700	0.01832(8)	4.1	0.0751(3)
800	0.00962(3)	6.6	0.0636(2)

TABLE X. Results for parton-level generation with rudimentary cuts for points which are excluded by monojet searches in [86]. Other values are set to $m_H = m_{H^\pm} = m_A = 600 \text{ GeV}$, $m_\chi = 1 \text{ GeV}$, $\cos(\beta - \alpha) = 0$, $\lambda_3 = \lambda_{P_1} = \lambda_{P_2} = 3$, $y_\chi = 1$, $\tan \beta = 1$. For $m_a \geq 500 \text{ GeV}$, the heavy scalar masses have been set to 1 TeV . The factor has been taken from HEPData [87]. The last column gives the actual exclusion cross section.

which corresponds to a 2σ limit. Direct detection bounds are compared to maximal cross section values $\sigma_{\text{max}}^{\text{Xenon1T}}(m_\chi)$ using XENON1T result[94], which we implemented in terms of an approximation function¹¹. Note we rescale bounds from direct detection according to

$$\sigma_{\text{max}}(m_{\chi,i}, \Omega_i) = \sigma_{\text{max}}^{\text{Xenon1T}}(m_\chi) \frac{0.1224}{\Omega_i}, \quad (17)$$

where $m_{\chi,i}$, Ω_i refer to the dark matter and relic density of the specific parameter point i tested here.

IV. SCAN SETUP AND RESULTS

A. Scan setup

The above constraints are implemented using an interplay of private and publicly available codes in several steps. We discuss these in the following. This also means that, as bounds are implemented successively, subsequent constraints are imposed on the subset of parameter points which have passed previous constraints.

1. In a first step, we impose perturbativity, positivity, and perturbative unitarity constraints as discussed in section III A. We also set a lower limit on $\tan \beta$ from the fit function for $B \rightarrow X_s \gamma$ derived in [54, 56].

¹¹ The numerical values have been obtained using the Phenodata database [95].

2. Points passing these bounds are then passed on to Sphenon, which is used for the calculation of limits from electroweak oblique parameters, $B_s \rightarrow \mu^+ \mu^-$, ΔM_s , as well as the total widths for all particles. These values are confronted with the experimental constraints discussed in section III B.
3. The remaining parameter points are now passed through HiggsBounds and HiggsSignals, for comparison with null-results from experimental searches as well as Higgs signal strength measurements which are contained in these tools.
4. We then calculate the relic density as well as direct detection constraints, which are discussed in section III D.
5. Parameter points which have passed all remaining constraints are confronted with the collider bounds presented in section III C.

Our initial scan ranges are determined by a number of prescans to determine regions of parameter space that are highly populated, while still rendering relatively low masses up to 1 TeV. In particular, we set

$$\begin{aligned}
&\sin \theta \in [-1; 0.8]; \cos(\beta - \alpha) \in [-0.08; 0.1]; \tan \beta \in [0.52; 9], \\
&m_H \in [500; 1000] \text{ GeV}, m_A \in [600; 1000] \text{ GeV}, m_{H^\pm} \in [800; 1000] \text{ GeV}, \\
&m_a \in [0; m_A], m_\chi \in [0, m_a], \\
&y_\chi \in [-\pi; \pi], \lambda_{P_1} \in [0; 10], \lambda_{P_2} \in [0; 4\pi], \lambda_3 \in [-2; 4\pi].
\end{aligned} \tag{18}$$

The values of $m_h = 125 \text{ GeV}$ and $v = 246 \text{ GeV}$ are set according to measurements of the Higgs boson mass as well as precision measurements. Note the above choices do not imply that values outside the above regions are strictly forbidden (apart from bounds we will discuss explicitly below), but these were found to render a relatively large acceptance rate for the scan discussed above. We furthermore apply the following relations between masses

$$\begin{aligned}
&m_A - m_H \in [-300; 400] \text{ GeV}, m_{H^\pm} - m_H \in [-150; 300] \text{ GeV}, m_A - m_{H^\pm} \in [-200; 200] \text{ GeV}, \\
&m_a < m_H + 400 \text{ GeV}, \quad m_a < m_{H^\pm} + 200 \text{ GeV}, \quad m_\chi < m_H - 200 \text{ GeV}, \\
&m_\chi < m_A - 300 \text{ GeV}, \quad m_\chi < m_{H^\pm} - 400 \text{ GeV} \quad m_\chi < m_a/2 + 50 \text{ GeV},
\end{aligned}$$

which were superimposed on the original scan ranges¹². Note that a priori also points outside the above regions were allowed; these were chosen to optimize the selections process imposed by cuts.

Note that the fit for $B \rightarrow X_s \gamma$ implies a lower bound on m_{H^\pm} of $\sim 800 \text{ GeV}$ ¹³.

¹² We obviously adjusted ranges such that all $m_i \geq 0 \text{ GeV}$.

¹³ We are aware that using these observables in a fit rather than as hard bounds might weaken some of the constraints discussed here, as e.g. discussed in [96] for a normal THDM. This is however beyond the scope of the current work.

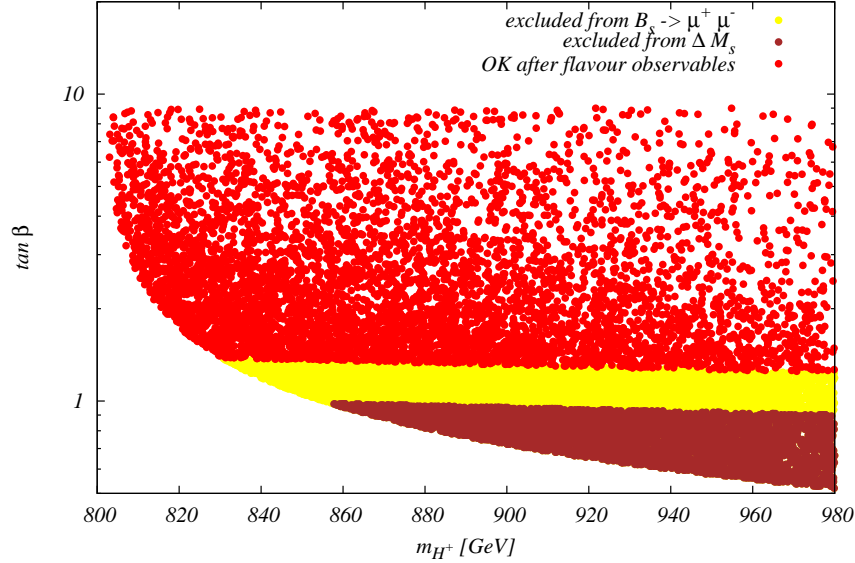


FIG. 1. Exclusion in the $(m_{H^\pm}, \tan \beta)$ plane after applying flavour constraints. The lower bound for $m_{H^\pm} \leq 850$ GeV is set by the bound on $B \rightarrow X_s \gamma$ as discussed in section III B.

B. Scan results

In the following, we discuss the resulting constraints on the parameter space of the THDMa. Note that not all bounds discussed above lead to a direct limit in a two-dimensional parameter plane. In case the effects can be displayed in such a simple way, we discuss them explicitly.

We generate ~ 30000 parameter points in the first step of the above scan. Application of bounds in step 2 includes e.g. constraints from flavour-physics in the $m_{H^\pm}, \tan \beta$ plane. Results from flavour constraints in the $m_{H^\pm}, \tan \beta$ plane are shown in figure 1, where similar results have been obtained e.g. in [52, 53, 97]¹⁴

¹⁴ Note the newest result from the LHC experimental combination for $B_s \rightarrow \mu^+ \mu^-$ [57] increases the discrepancy between experimental result and theory prediction, leading to a larger exclusion region. In the mass range considered here, we found the limit can be approximated by requiring $\tan \beta \geq 2.15302 - 0.000930233 \frac{m_{H^\pm}}{\text{GeV}}$. Furthermore, in [52], the ΔM_s bound is not shown in the figure for flavour constraints. However, similar results are obtained as well. TR wants to thank the GFitter authors for clarifying this point.

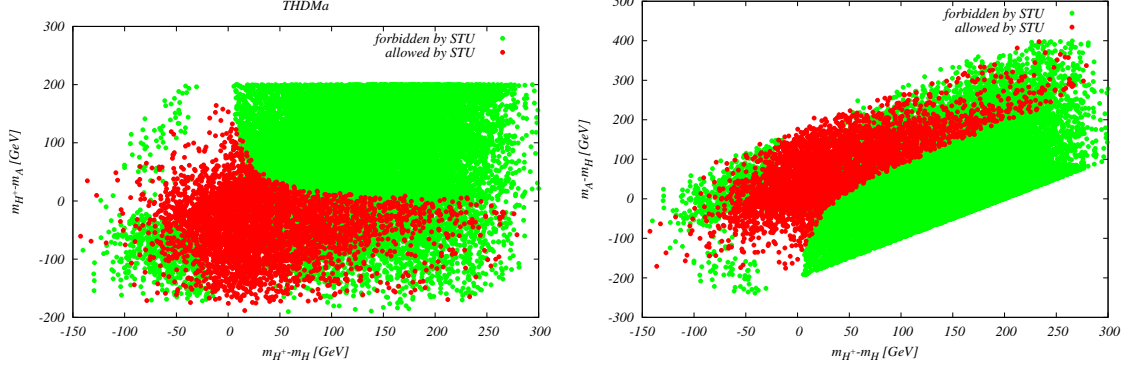


FIG. 2. Exclusions in the $(m_{H^\pm} - m_H, m_{H^\pm} - m_A)$ (left) and $(m_{H^\pm} - m_H, m_H - m_A)$ (right) planes from oblique parameters. We see that regions where both displayed mass differences are large are excluded by the oblique parameters.

After the bounds imposed by theory, the only constraints we find from widths are points which violate (9). This basically rules out all points with $m_a \leq 62.5$ GeV, as the $h \rightarrow aa$ decay becomes dominant and can lead to large partial widths¹⁵. All other mass ratios are $\Gamma/m \lesssim 28\%$ for all points that fulfill theory constraints, and maximally around 24% for Γ_A/m_A after width bounds are included. As an example, the point with the largest allowed ratio features a dominant branching ratio for $A \rightarrow ha$, mediated via relatively large $\tan\beta \sim 8.1$, $\lambda_{P_2} \sim 11.6$ values and masses $m_A = 847$ GeV, $m_a = 298$ GeV. For large values of Γ_H/m_H , typically $H \rightarrow aZ$ and $H \rightarrow t\bar{t}$ are dominant, with $m_H \gtrsim 800$ GeV, $|\sin\theta| \sim 0.35 - 0.65$. Large widths for a typically stem from large $|y_\chi| \sim 1.8$ and small $|\sin\theta| \lesssim 0.2$ values, corresponding to the coupling determining the $a \rightarrow \chi\bar{\chi}$ decay [4]. Electroweak precision observables, on the other hand, have an impact on the allowed mass splittings, such that for example regions with $|m_{H^\pm} - m_A| \gtrsim 190$ GeV are basically forbidden. In fact, we see largest deviations in the oblique parameters trace back to too large absolute values of the T-parameter, i.e. $T \lesssim -0.03$, where largest values stem from $|m_{H^\pm} - m_H| \gtrsim 250$ GeV. Such deviations typically stem from new physics contributions to gauge-boson propagators, therefore being sensitive to mass differences. As an example, we show the exclusion in the $(m_{H^\pm} - m_H, m_{H^\pm} - m_A)$ and $(m_{H^\pm} - m_H, m_H - m_A)$ planes in figure 2. Another interesting parameter plane is given by $(m_a, |\sin\theta|)$, where the oblique parameters also set a clear limit, see figure 3. We also investigate how our results compare to the ones obtained in the THDM limit, where a is decoupled. This can be achieved setting $\sin\theta = \lambda_{P_1} = \lambda_{P_2} = 0$. We then compare the limits in the $(m_{H^\pm} - m_A, m_H - m_A)$ plane, cf. fig. 4. We see that the admixture of a leads to much weaker constraints on $m_{H^\pm} - m_A$. For the remaining constraints discussed in section III B, the identification of additional regions in two-dimensional parameter planes that are primarily affected is not straightforward.

¹⁵ Note that the respective coupling does not approach zero for $\sin\theta \rightarrow 0$, but is mediated via λ_{P_1} and λ_{P_2} , cf. e.g. the explicit form of the coupling given in [4].

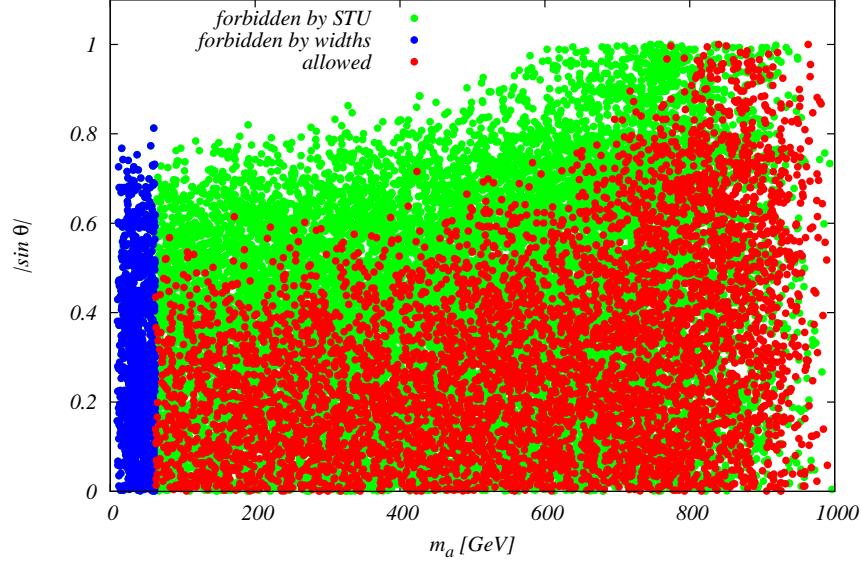


FIG. 3. Exclusion in the $(m_a, |\sin \theta|)$ plane from oblique parameters. Limits from setting an upper bound on the total width of the 125 GeV scalar (eqn. (9)) are also shown.

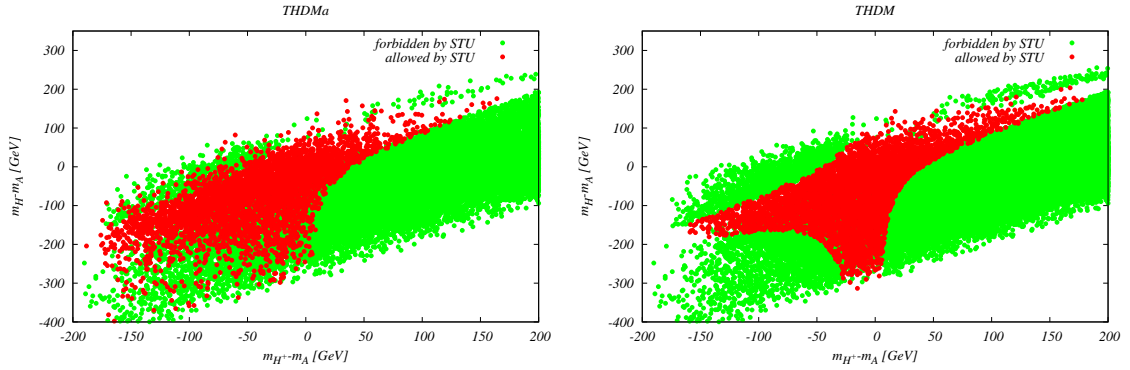


FIG. 4. Exclusions in the $(m_{H^\pm} - m_A, m_H - m_A)$ plane in the THDMa (left) and THDM (right) from oblique parameters; for the latter, $\sin \theta = \lambda_{P_1} = \lambda_{P_2} = 0$. The admixture of a releases the bounds, as expected.

We now turn to the effects of applying collider constraints via HiggsBounds/ HiggsSignals. As expected in THDMs and its extensions, only narrow stripes around $\cos(\beta - \alpha) = 0$ remain in agreement with current signal strength measurements (see e.g. [98, 99]).

Using the tools described above, we find the allowed/ forbidden areas in the $(\cos(\beta - \alpha), \tan \beta)$ plane as shown in figure 5¹⁶. Some points are additionally ruled out by $H/a \rightarrow \tau\tau$ [103],

¹⁶ Comparing to the results presented e.g. in [100, 101], we see that constraints for negative values of $\cos(\beta - \alpha)$ agree, while we find more stringent constraints for positive values. However, note that we use different approaches, and for example HiggsSignals makes use of the most recent constraints as well as STXS information [102]. We thank the authors of [100] for useful correspondence concerning this point.

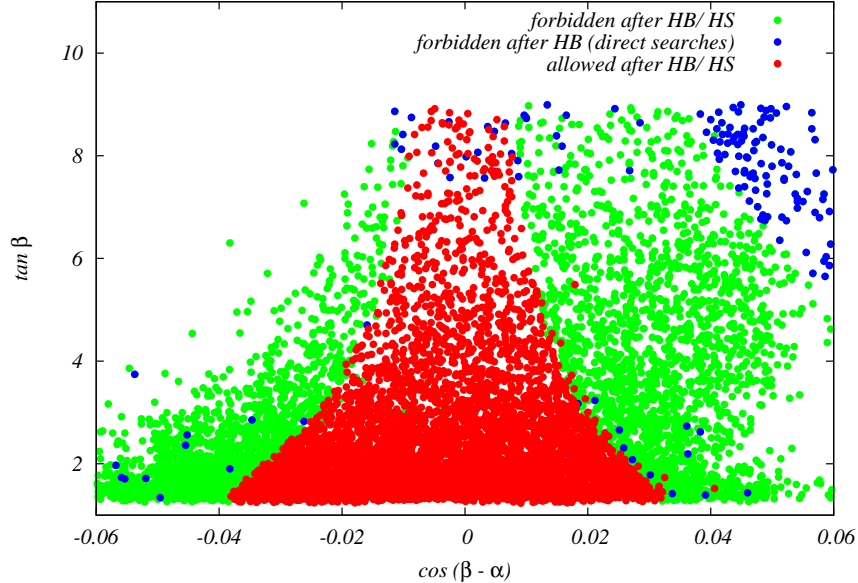


FIG. 5. Exclusion in the $\cos(\beta - \alpha), \tan \beta$ plane after HiggsBounds (HB) and HiggsSignals (HS).

$H \rightarrow h_{125}h_{125}$ [104] and $H \rightarrow aZ$ [105, 106] searches. Values of $\cos(\beta - \alpha) > 0.04$ and $\tan \beta \gtrsim 5$ are excluded from $h_{125} \rightarrow ZZ$ [107]. Points which are still allowed after the application of HiggsBounds and HiggsSignals are outside the region sensitive to the full Run 2 $A \rightarrow HZ$ search [108], assuming on-shell production and decay¹⁷. Furthermore, the region where $\cos(\beta - \alpha) \lesssim -0.05$, $\tan \beta \gtrsim 5$ is mainly ruled out from both perturbative unitarity and perturbativity.

Constraints from relic density, i.e. the requirement that eqn. (16) is fulfilled, depends on many parameters. In general, however, small values of $|m_a - 2m_\chi|$ can trigger efficient annihilation processes via the resonant s-channel diagram, and lead to relic density values between 10^{-6} and the upper bound. For larger mass differences $\mathcal{O}(200 \text{ GeV})$ or larger, basically all points are excluded. Dominant annihilation channels are $\chi\bar{\chi} \rightarrow b\bar{b}$ and $\chi\bar{\chi} \rightarrow t\bar{t}$, where the latter channel opens up for $m_a \gtrsim 2m_t$ and tends to lead to smaller values of relic density. We show the values of relic density as a function of the above mass difference in figure 6.

Similarly, for $\sin \theta \rightarrow 0$ annihilation cross sections tend to become small, such that relic density predictions exceed the value measured by the Planck collaboration, cf. eq. (16). We display the dependence on this variable in figure 6, where in addition color coding indicates the mass difference $m_a - 2m_\chi$.

Considering only points that pass the relic density constraints, we found that direct detection does not impose any additional constraints. A more detailed analysis, as e.g.

¹⁷ We tested this by comparing to cross sections for $pp \rightarrow A \rightarrow ZH$ production and successive decays $H \rightarrow b\bar{b}$ from figure 10 in that reference.

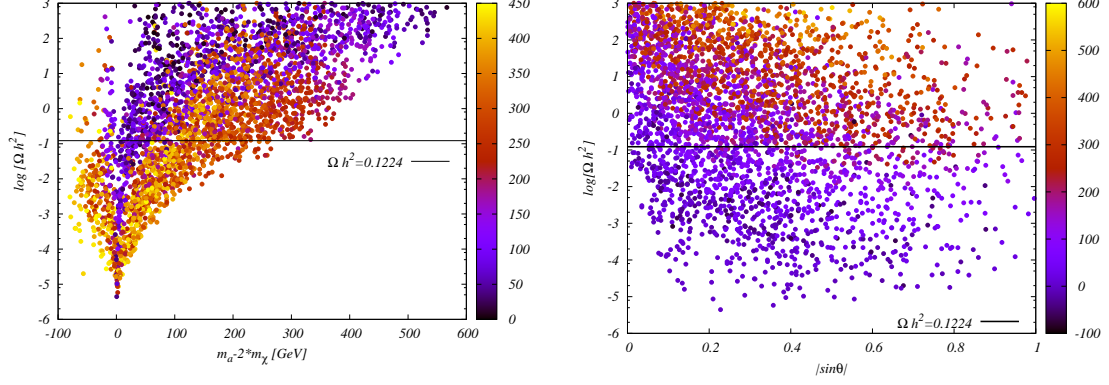


FIG. 6. *Left:* Relic density as a function of $m_a - 2m_\chi$, with the color coding referring to the mass of the DM candidate. Heavier m_χ tend to lead to smaller values of the relic density. *Right:* Relic density as a function of $|\sin \theta|$, with the color coding referring to the mass difference $m_a - 2m_\chi$. Lower values of $|\sin \theta|$ lead to smaller annihilation cross sections and therefore larger values of the relic density.

presented in [9, 12, 91, 92], could modify this statement. However, from figure 24 in [6], we see that these constraints are effective only for masses $m_a \lesssim 60$ GeV and additionally depend on the mixing angle. We have verified that the few points that feature this mass range are not excluded when comparing to the above figure. Further comments on the sensitivity of future direct detection experiments for this model can e.g. be found in [12].

Before discussing constraints from direct searches, we will briefly summarize the effects the bounds considered above have imposed on the original parameter space

- B-physics constraints set a lower bound on $\tan \beta$ as a function of m_{H^\pm} ; in general, $\tan \beta > 1$.
- Signal strength measurements reduced the available parameter space for $\cos(\beta - \alpha)$, such that now $\cos(\beta - \alpha) \in [-0.04; 0.04]$.
- Relic density reduced the available parameter space to regions where $m_a - 2m_\chi \in [-100; 300]$ GeV.
- Furthermore, oblique parameters reduce the allowed mass differences, especially in the THDM scalar sector.
- In the general scan, also the upper limits of m_a in dependence on m_H , m_{H^\pm} are reduced by more than 100 GeV. However, this is an artefact of the scan, and one can easily repopulate these regions in a more finetuned setup.
- We also see that $m_H > 550$ GeV, $m_A > 750$ GeV. In both cases, a large number of points are excluded from S, T, U observables, as these variables favour small mass

differences between the new scalars. If we force $m_A \leq 750$ GeV, for example, out of 1000 points only one survives which has very degenerate m_H, m_{H^\pm} masses, differing on the permill level. If we force $m_H \leq 550$ GeV, more points survive, which feature a small m_{H^\pm}, m_A difference, typically $\lesssim 10\%$ difference, as well as small mass differences $|m_a - 2m_\chi| \lesssim 120$ GeV. In a general, non-finetuned scan, the lower bound on m_{H^\pm} forces the mass scale of H, A to be $\gtrsim 530 - 550$ GeV.

All other parameters still populate the original regions set in eqn. (18).

Regarding direct collider constraints as discussed in section III C, we find the following results

- The strongest constraints stem from $h + \cancel{E}_\perp$ searches presented in [32], cutting out around $\sim 28\%$ of the leftover parameter space. As we let all parameters float freely, limits in 2-dimensional planes are not straightforward. Using our approach, only points for which $m_a - 2m_\chi \geq 0$ are affected. Furthermore, points where $m_\chi \geq 400$ GeV are not affected. This however is e.g. due to a strong correlation between m_χ and m_a , which in turn influences the mass difference $m_A - m_a$ and the $A \rightarrow h a$ branching ratio.
- The $\ell\ell + \cancel{E}_\perp$ searches cut out roughly 9% of the available parameter space. As in [22], regions with $m_a \lesssim 500$ GeV are mainly affected. However, as we scan over all parameters, also many points for which $m_a \lesssim 500$ GeV are still allowed. In addition, the branching ratio for $H \rightarrow a Z$ swiftly goes to 0 when $m_H - m_a \rightarrow m_Z$, and only has reasonably large values when $m_H - m_a \gtrsim 200$ GeV, so that only points obeying this mass hierarchy are excluded. Similarly, as the above branching ratio $\sim \sin^2 \theta$, we found that points for which $|\sin \theta| \lesssim 0.15$ are not excluded.
- The bounds from the $pp \rightarrow H^+ \bar{t} b, H^+ \rightarrow \bar{t} b$ searches [25] do not constrain the parameter space here, as production cross sections for the process $pp \rightarrow H^+ \bar{t} b$ are $\mathcal{O}(10^{-2})$ pb. This can be traced back to the lower limit on $\tan \beta$ from B-physics observables, cf. fig 1. The same holds for searches in the same production mode, but with different final states [30].
- Searches for $t \bar{t} + \cancel{E}_\perp$ cut out a relatively small region of parameter space, $\sim 1\%$, in the range where $m_a \lesssim 300$ GeV, $m_a - 2m_\chi \in [0; 40]$ GeV, $\tan \beta \lesssim 2$. As before, several parameters contribute, so one also finds allowed points within the regions mentioned above. All of these are also subject to at least one other constraint from the searches mentioned above.
- None of the points is excluded by the $W^+ \bar{t} + \cancel{E}_\perp / W^- t + \cancel{E}_\perp, b \bar{b} + \cancel{E}_\perp$ and monojet searches considered here.

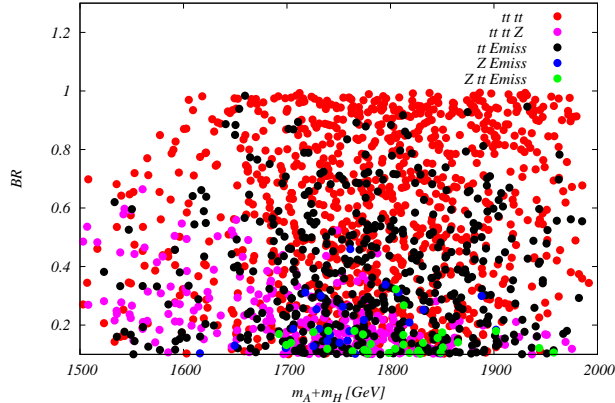


FIG. 7. Combined branching ratios for HA final states, as a function of the mass sum.

V. PREDICTIONS FOR e^+e^- COLLIDERS

Out of the remaining parameter space, we now investigate the magnitude of expected rates at possible future e^+e^- colliders. In the limit where $\sin \theta \rightarrow 0$, we recover the decoupling scenario of a standard THDM. It is therefore interesting whether we can find regions in parameter space where novel signatures, and explicitly final states with missing energy, give the largest rates.

If we focus on the neutral sector and pair-production processes, possible final states are given by ha , hA , HA , Ha . For the first two processes, the sum of masses remains $\lesssim 1$ TeV, so colliders with a center-of-mass energy in that range might be relevant. For the latter two, on the other hand, masses can range above 1 TeV, and we can consider cross sections at a 3 TeV collider.

Note that h [H] A production in a THDM is mediated mainly via Z-boson exchange in the s-channel, where the corresponding coupling is proportional to $\cos(\beta - \alpha)$ [$\sin(\beta - \alpha)$] respectively. As $\cos(\beta - \alpha)$ is heavily constrained, the corresponding cross-sections are quite small, reaching $\mathcal{O}(10^{-3}\text{fb})$. Therefore, we will here concentrate on $HA(a)$ production and decay. For this channel, we find that at a 3 TeV collider, production cross-sections can reach up to 1 fb, where largest cross section values are achieved for $m_A + m_H \sim 1400$ GeV. Dominant decay modes for such points are displayed in figure 7. Decays without missing energy lead to $t\bar{t}t\bar{t}$ and $t\bar{t}t\bar{t}Z$ final states, where the first is dominant in large regions of parameter space. The first decay mode that is novel with respect to standard THDMs is the $t\bar{t} + \cancel{E}$ final state. In order to identify regions where this state dominates, we show the expected $t\bar{t}t\bar{t}$ and $t\bar{t} + \cancel{E}$ cross sections in figure 8, where in the right plot we additionally include contributions mediated via Ha production. We see that indeed we can identify regions where $t\bar{t} + \cancel{E}$ dominates and renders the largest rates. As an example, we here list

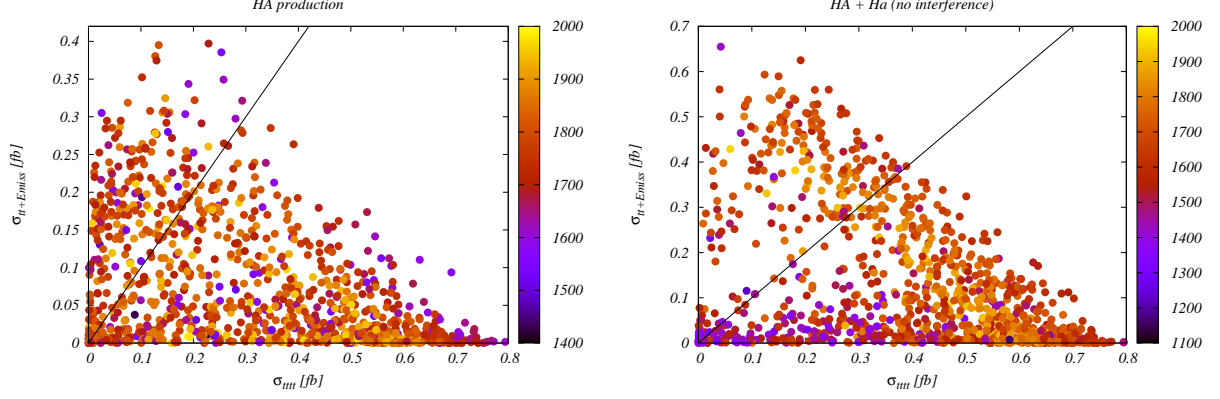


FIG. 8. Production cross sections for $t\bar{t}t\bar{t}$ and $t\bar{t} + \cancel{E}$ final states, using a factorized approach. (Left:) via HA and (right:) via $HA + Ha$ production. Color coding refers to the mass scale, which is defined as $m_H + m_A$ (left)/ $m_H + 0.5 \times (m_A + m_a)$ (right), respectively.

the parameters of the "best point":

$$\begin{aligned}
 \sin \theta &= -0.626, \cos(\beta - \alpha) = 0.0027, \tan \beta = 3.55 \\
 m_H &= 643 \text{ GeV}, m_A = 907 \text{ GeV}, m_{H^\pm} = 814 \text{ GeV}, \\
 m_a &= 653 \text{ GeV}, m_\chi = 277 \text{ GeV}, \\
 y_\chi &= -1.73, \lambda_{P_1} = 0.18, \lambda_{P_2} = 2.98, \lambda_3 = 8.63.
 \end{aligned} \tag{19}$$

The total widths are given by $\Gamma_H = 2.41 \text{ GeV}$, $\Gamma_A = 52.5 \text{ GeV}$, $\Gamma_a = 26.5 \text{ GeV}$, $\Gamma_{H^\pm} = 12.1 \text{ GeV}$, rendering all width/ mass ratios $\lesssim 6 \%$. The production cross sections at 3 TeV are given by $\sigma_{HA} = 0.512 \text{ fb}$, $\sigma_{Ha} = 0.390 \text{ fb}$. The H decays to $t\bar{t}$ with a branching ratio of 93%, while $\chi\bar{\chi}$ final states have branching ratios of 64%/95% for A/a , respectively. This leads to an overall estimated production cross section of around 0.65 fb, using factorization and neglecting possible interference effects. The next step in this investigation would be a detailed simulation of signal and background in a CLIC-like environment, as e.g. performed in [109, 110] for the Inert Doublet Model. This is in the line of future work.

VI. SUMMARY AND OUTLOOK

In this work, we for the first time presented a scan for the THDMa that lets all 12 free parameters of that model float freely, within ranges that were chosen to optimize scan performance. We have identified regions in parameter space that survive all current theoretical and experimental constraints, and provided a first estimate of possible production cross sections within this model at future e^+e^- facilities, with a focus on signatures not present in a standard THDM. We have included direct LHC search results using a simplified approach, with maximal cross sections as an upper limit. Such searches typically constrain

the low-mass regions of parameter space, where the dark sector masses are $\lesssim 500$ GeV, as well as regions with mixings $|\sin\theta| \gtrsim 0.15$. In general, however, clear boundaries in two-dimensional planes are not easy to identify. An exception are constraints from B-physics observables, that especially impose a lower limit on the charged mass ~ 800 GeV that varies with $\tan\beta$. Furthermore, constraints from electroweak precision observables in the form of oblique parameters pose relatively strong constraints on the mass differences in the THDMa scalar sector for novel scalars, leading to a general lower mass scale ~ 500 GeV. Requiring the relic density to lie below the current experimental measurement furthermore poses strong constraints on $|m_a - 2m_\chi|$.

We consider this work as a first step towards a more detailed analysis of this model. This includes more detailed recasts of the current LHC experimental results, including possible forecasts for HL-LHC sensitivity, as well as more detailed investigations at future lepton machines, as e.g. CLIC or possible muon-colliders. First estimates for the former show that the most promising novel channel could be $t\bar{t} + \cancel{E}$ in a CLIC-like scenario with a 3 TeV center-of-mass energy.

Finally, in view of recent events [111], one might wonder whether the anomalous magnetic momentum of the muon can be explained by the model discussed here. Contributions should be similar to the ones of a general THDM of type II, as e.g. discussed in [112, 113], with additional contributions of the second pseudoscalar a , including appropriate rescaling. However, from the above work it becomes obvious that pseudoscalar masses would have to be light, $\lesssim 200$ GeV, with additionally relatively large $\tan\beta$ values $\gtrsim 15$, in order to account for the observed experimental value. Such points have not been included in our analysis here. A quick check using the next-to-leading order approximation given in [114] shows that maximal values of $\Delta a_\mu^{\text{BSM}} \sim 2.5 \times 10^{-12}$ can be achieved with e.g. the points which pass all other (including experimental LHC) constraints, which is around three orders of magnitude lower than the observed discrepancy. In [52], regions are shown in the $(m_{H^\pm}, \tan\beta)$ plane; here, for charged masses $\gtrsim 800$ GeV, $\tan\beta \gtrsim 7$ seems to be required for 68% confidence level agreement with the result from [115]. This could a priori be an interesting region to investigate, which we will leave for future work.

ACKNOWLEDGEMENTS

The author wants to sincerely thank J. Kalinowski, W. Kotlarski, D. Sokolowska, and A.F. Zarnecki for useful discussions in the beginning of this project, and especially W. Kotlarski for help with the setup of the Sarah/ Spheno interface. Further thanks go to M. Misiak and U. Nierste for discussions regarding bounds from B-physics observables, and M. Goodsell as well as the authors of [12] for advice. This research was supported in parts by the National Science Centre, Poland, the HARMONIA project under contract UMO-2015/18/M/ST2/00518 (2016-2021), and the OPUS project under contract UMO-

Appendix A: Potential parameters

The potential parameters can be expressed in terms of the free input parameters as follows:

$$\mu_3 = \frac{1}{2}s_{2\alpha}(m_h^2 - m_H^2) - m_{H^\pm}^2 s_{2\beta} + \frac{v^2}{2}\lambda_3 s_{2\beta} \quad (\text{A1})$$

$$\lambda_1 = \frac{s_\alpha s_{\alpha+\beta}}{2v^2 c_\beta^3} m_h^2 + \frac{c_\alpha c_{\alpha+\beta}}{2v^2 c_\beta^3} m_H^2 - \frac{t_\beta^2}{v^2} m_{H^\pm}^2 + \frac{t_\beta^2}{2} \lambda_3 \quad (\text{A2})$$

$$\lambda_2 = \frac{c_\alpha s_{\alpha+\beta}}{2v^2 s_\beta^3} m_h^2 - \frac{s_\alpha c_{\alpha+\beta}}{2v^2 s_\beta^3} m_H^2 - \frac{1}{v^2 t_\beta^2} m_{H^\pm}^2 + \frac{1}{2t_\beta^2} \lambda_3 \quad (\text{A3})$$

$$\lambda_5 = -\frac{1}{2v^2} \left(-2m_{H^\pm}^2 + v^2 \lambda_3 + m_A^2 c_\theta^2 + m_a^2 s_\theta^2 + (m_h^2 - m_H^2) \frac{s_{2\alpha}}{s_{2\beta}} \right) \quad (\text{A4})$$

$$\lambda_4 = \frac{1}{v^2} \left(m_A^2 c_\theta^2 + m_a^2 s_\theta^2 - v^2 \lambda_3 + (m_H^2 - m_h^2) \frac{s_{2\alpha}}{s_{2\beta}} \right) \quad (\text{A5})$$

$$b_p = \frac{(m_a^2 - m_A^2) c_\theta s_\theta}{v} \quad (\text{A6})$$

$$m_P^2 = m_a^2 c_\theta^2 + m_A^2 s_\theta^2 - v^2 (\lambda_{p1} c_\beta^2 + \lambda_{p2} s_\beta^2) \quad (\text{A7})$$

-
- [1] Seyda Ipek, David McKeen, and Ann E. Nelson. A Renormalizable Model for the Galactic Center Gamma Ray Excess from Dark Matter Annihilation. *Phys. Rev.*, D90(5):055021, 2014, 1404.3716.
 - [2] Jose Miguel No. Looking through the pseudoscalar portal into dark matter: Novel mono-Higgs and mono-Z signatures at the LHC. *Phys. Rev.*, D93(3):031701, 2016, 1509.01110.
 - [3] Dorival Goncalves, Pedro A. N. Machado, and Jose Miguel No. Simplified Models for Dark Matter Face their Consistent Completions. *Phys. Rev.*, D95(5):055027, 2017, 1611.04593.
 - [4] Martin Bauer, Ulrich Haisch, and Felix Kahlhoefer. Simplified dark matter models with two Higgs doublets: I. Pseudoscalar mediators. *JHEP*, 05:138, 2017, 1701.07427.
 - [5] Patrick Tunney, Jose Miguel No, and Malcolm Fairbairn. Probing the pseudoscalar portal to dark matter via $\bar{b}bZ(\rightarrow \ell\ell)+\cancel{E}_T$: From the LHC to the Galactic Center excess. *Phys. Rev.*, D96(9):095020, 2017, 1705.09670.
 - [6] Tomohiro Abe et al. LHC Dark Matter Working Group: Next-generation spin-0 dark matter models. *Phys. Dark Univ.*, 27:100351, 2020, 1810.09420.

- [7] Priscilla Pani and Giacomo Polesello. Dark matter production in association with a single top-quark at the LHC in a two-Higgs-doublet model with a pseudoscalar mediator. *Phys. Dark Univ.*, 21:8–15, 2018, 1712.03874.
- [8] Ulrich Haisch, Jernej F. Kamenik, Augustinas Malinauskas, and Michael Spira. Collider constraints on light pseudoscalars. *JHEP*, 03:178, 2018, 1802.02156.
- [9] Tomohiro Abe, Motoko Fujiwara, and Junji Hisano. Loop corrections to dark matter direct detection in a pseudoscalar mediator dark matter model. *JHEP*, 02:028, 2019, 1810.01039.
- [10] Ulrich Haisch and Giacomo Polesello. Searching for dark matter in final states with two jets and missing transverse energy. *JHEP*, 02:128, 2019, 1812.08129.
- [11] Ulrich Haisch and Giacomo Polesello. Searching for production of dark matter in association with top quarks at the LHC. *JHEP*, 02:029, 2019, 1812.00694.
- [12] Tomohiro Abe, Motoko Fujiwara, Junji Hisano, and Yutaro Shoji. Maximum value of the spin-independent cross section in the 2HDM+a. *JHEP*, 01:114, 2020, 1910.09771.
- [13] J. M. Butterworth, M. Habedank, P. Pani, and A. Vaitkus. A study of collider signatures for two Higgs doublet models with a Pseudoscalar mediator to Dark Matter. *SciPost Phys. Core*, 4:003, 2021, 2009.02220.
- [14] Giorgio Arcadi, Giorgio Busoni, Thomas Hugle, and Valentin Titus Tenorth. Comparing 2HDM + Scalar and Pseudoscalar Simplified Models at LHC. *JHEP*, 06:098, 2020, 2001.10540.
- [15] Spyros Argyropoulos, Oleg Brandt, and Ulrich Haisch. Collider Searches for Dark Matter through the Higgs Lens. *Symmetry*, 2021:13, 9 2021, 2109.13597.
- [16] Morad Aaboud et al. Search for dark matter produced in association with bottom or top quarks in $\sqrt{s} = 13$ TeV pp collisions with the ATLAS detector. *Eur. Phys. J., C*78(1):18, 2018, 1710.11412.
- [17] Albert M Sirunyan et al. Search for dark matter produced in association with a Higgs boson decaying to a pair of bottom quarks in proton–proton collisions at $\sqrt{s} = 13$ TeV. *Eur. Phys. J. C*, 79(3):280, 2019, 1811.06562.
- [18] Morad Aaboud et al. Search for Higgs boson decays into a pair of light bosons in the $b\bar{b}\mu\mu$ final state in pp collision at $\sqrt{s} = 13$ TeV with the ATLAS detector. *Phys. Lett., B*790:1–21, 2019, 1807.00539.
- [19] Morad Aaboud et al. Search for Higgs boson decays to beyond-the-Standard-Model light bosons in four-lepton events with the ATLAS detector at $\sqrt{s} = 13$ TeV. *JHEP*, 06:166, 2018, 1802.03388.
- [20] Morad Aaboud et al. Constraints on mediator-based dark matter and scalar dark energy models using $\sqrt{s} = 13$ TeV pp collision data collected by the ATLAS detector. *JHEP*, 05:142, 2019, 1903.01400.
- [21] Albert M Sirunyan et al. Search for dark matter particles produced in association with a Higgs boson in proton-proton collisions at $\sqrt{s} = 13$ TeV. *JHEP*, 03:025, 2020, 1908.01713.

- [22] Albert M Sirunyan et al. Search for dark matter produced in association with a leptonically decaying Z boson in proton-proton collisions at $\sqrt{s} = 13$ TeV. *Eur. Phys. J.*, C81(1):13, 2021, 2008.04735.
- [23] Georges Aad et al. Search for dark matter produced in association with a single top quark in $\sqrt{s} = 13$ TeV pp collisions with the ATLAS detector. *Eur. Phys. J. C*, 81:860, 2021, 2011.09308.
- [24] Georges Aad et al. Search for Higgs boson decays into two new low-mass spin-0 particles in the $4b$ channel with the ATLAS detector using pp collisions at $\sqrt{s} = 13$ TeV. *Phys. Rev.*, D102:112006, 2020, 2005.12236.
- [25] Georges Aad et al. Search for dijet resonances in events with an isolated charged lepton using $\sqrt{s} = 13$ TeV proton-proton collision data collected by the ATLAS detector. *JHEP*, 06:151, 2020, 2002.11325.
- [26] Georges Aad et al. Search for new phenomena with top quark pairs in final states with one lepton, jets, and missing transverse momentum in pp collisions at $\sqrt{s} = 13$ TeV with the ATLAS detector. *JHEP*, 04:174, 2021, 2012.03799.
- [27] Georges Aad et al. Search for new phenomena in final states with b -jets and missing transverse momentum in $\sqrt{s} = 13$ TeV pp collisions with the ATLAS detector. *JHEP*, 05:093, 2021, 2101.12527.
- [28] Georges Aad et al. Search for new phenomena in events with two opposite-charge leptons, jets and missing transverse momentum in pp collisions at $\sqrt{s} = 13$ TeV with the ATLAS detector. *JHEP*, 04:165, 2021, 2102.01444.
- [29] Georges Aad et al. Search for Higgs boson decays into a pair of pseudoscalar particles in the $b\bar{b}\mu\mu$ final state with the ATLAS detector in pp collisions at $\sqrt{s} = 13$ TeV. 10 2021, 2110.00313.
- [30] Georges Aad et al. Search for charged Higgs bosons decaying into a top quark and a bottom quark at $\sqrt{s} = 13$ TeV with the ATLAS detector. *JHEP*, 06:145, 2021, 2102.10076.
- [31] Georges Aad et al. Search for dark matter in events with missing transverse momentum and a Higgs boson decaying into two photons in pp collisions at $\sqrt{s} = 13$ TeV with the ATLAS detector. *JHEP*, 10:013, 2021, 2104.13240.
- [32] Georges Aad et al. Search for dark matter produced in association with a Standard Model Higgs boson decaying into b -quarks using the full Run 2 dataset from the ATLAS detector. 8 2021, 2108.13391.
- [33] Georges Aad et al. Search for associated production of a Z boson with an invisibly decaying Higgs boson or dark matter candidates at $\sqrt{s} = 13$ TeV with the ATLAS detector. 11 2021, 2111.08372.
- [34] Combination and summary of ATLAS dark matter searches using 139 fb⁻¹ of $\sqrt{s} = 13$ TeV $p p$ collision data and interpreted in a two-Higgs-doublet model with a pseudoscalar mediator. Technical report, CERN, Geneva, Aug 2021. All figures including auxiliary figures are

- available at <https://atlas.web.cern.ch/Atlas/GROUPS/PHYSICS/CONFNOTES/ATLAS-CONF-2021-036>.
- [35] Projection of the Mono-Z search for dark matter to the HL-LHC. Technical Report CMS-PAS-FTR-18-007, CERN, Geneva, 2018.
 - [36] ATLAS sensitivity to Two-Higgs-Doublet models with an additional pseudoscalar exploiting four top quark signatures with 3ab^{-1} of $\sqrt{s} = 14$ TeV proton-proton collisions. Technical report, CERN, Geneva, Nov 2018. All figures including auxiliary figures are available at <https://atlas.web.cern.ch/Atlas/GROUPS/PHYSICS/PUBNOTES/ATL-PHYS-PUB-2018-027>.
 - [37] ATLAS sensitivity to dark matter produced in association with heavy quarks at the HL-LHC. Technical report, CERN, Geneva, Nov 2018. All figures including auxiliary figures are available at <https://atlas.web.cern.ch/Atlas/GROUPS/PHYSICS/PUBNOTES/ATL-PHYS-PUB-2018-036>.
 - [38] Xabier Cid Vidal et al. Report from Working Group 3. *CERN Yellow Rep. Monogr.*, 7:585–865, 2019, 1812.07831.
 - [39] G. C. Branco, P. M. Ferreira, L. Lavoura, M. N. Rebelo, Marc Sher, and Joao P. Silva. Theory and phenomenology of two-Higgs-doublet models. *Phys. Rept.*, 516:1–102, 2012, 1106.0034.
 - [40] Werner Porod. SPheno, a program for calculating supersymmetric spectra, SUSY particle decays and SUSY particle production at e+ e- colliders. *Comput. Phys. Commun.*, 153:275–315, 2003, hep-ph/0301101.
 - [41] W. Porod and F. Staub. SPheno 3.1: Extensions including flavour, CP-phases and models beyond the MSSM. *Comput. Phys. Commun.*, 183:2458–2469, 2012, 1104.1573.
 - [42] F. Staub. SARAH. 2008, 0806.0538.
 - [43] Florian Staub. From Superpotential to Model Files for FeynArts and CalcHep/CompHep. *Comput. Phys. Commun.*, 181:1077–1086, 2010, 0909.2863.
 - [44] Florian Staub. Automatic Calculation of supersymmetric Renormalization Group Equations and Self Energies. *Comput. Phys. Commun.*, 182:808–833, 2011, 1002.0840.
 - [45] Florian Staub. SARAH 3.2: Dirac Gauginos, UFO output, and more. *Comput. Phys. Commun.*, 184:1792–1809, 2013, 1207.0906.
 - [46] Florian Staub. SARAH 4 : A tool for (not only SUSY) model builders. *Comput. Phys. Commun.*, 185:1773–1790, 2014, 1309.7223.
 - [47] Guido Altarelli and Riccardo Barbieri. Vacuum polarization effects of new physics on electroweak processes. *Phys. Lett.*, B253:161–167, 1991.
 - [48] Michael E. Peskin and Tatsu Takeuchi. A New constraint on a strongly interacting Higgs sector. *Phys. Rev. Lett.*, 65:964–967, 1990.
 - [49] Michael E. Peskin and Tatsu Takeuchi. Estimation of oblique electroweak corrections. *Phys. Rev.*, D46:381–409, 1992.

- [50] M. Baak, J. Cúth, J. Haller, A. Hoecker, R. Kogler, K. Mönig, M. Schott, and J. Stelzer. The global electroweak fit at NNLO and prospects for the LHC and ILC. *Eur. Phys. J.*, C74:3046, 2014, 1407.3792.
- [51] <http://project-gfitter.web.cern.ch/project-gfitter/>.
- [52] Johannes Haller, Andreas Hoecker, Roman Kogler, Klaus Moenig, Thomas Peiffer, and Joerg Stelzer. Update of the global electroweak fit and constraints on two-Higgs-doublet models. *Eur. Phys. J.*, C78(8):675, 2018, 1803.01853.
- [53] A. Arbey, F. Mahmoudi, O. Stal, and T. Stefaniak. Status of the Charged Higgs Boson in Two Higgs Doublet Models. *Eur. Phys. J.*, C78(3):182, 2018, 1706.07414.
- [54] M. Misiak, Abdur Rehman, and Matthias Steinhauser. Towards $\overline{B} \rightarrow X_s \gamma$ at the NNLO in QCD without interpolation in m_c . *JHEP*, 06:175, 2020, 2002.01548.
- [55] M. Misiak et al. Updated NNLO QCD predictions for the weak radiative B-meson decays. *Phys. Rev. Lett.*, 114(22):221801, 2015, 1503.01789.
- [56] M. Misiak. Private communication.
- [57] Combination of the ATLAS, CMS and LHCb results on the $B_{(s)}^0 \rightarrow \mu^+ \mu^-$ decays. Technical Report ATLAS-CONF-2020-049, CERN, Geneva, Aug 2020.
- [58] Xiao-Dong Cheng, Ya-Dong Yang, and Xing-Bo Yuan. Revisiting $B_s \rightarrow \mu^+ \mu^-$ in the two-Higgs doublet models with Z_2 symmetry. *Eur. Phys. J.*, C76(3):151, 2016, 1511.01829.
- [59] Martin Beneke, Christoph Bobeth, and Robert Szafron. Power-enhanced leading-logarithmic QED corrections to $B_q \rightarrow \mu^+ \mu^-$. *JHEP*, 10:232, 2019, 1908.07011.
- [60] Yasmine Sara Amhis et al. Averages of b-hadron, c-hadron, and τ -lepton properties as of 2018. *Eur. Phys. J.*, C81(3):226, 2021, 1909.12524.
- [61] A. Lenz, U. Nierste, J. Charles, S. Descotes-Genon, A. Jantsch, C. Kaufhold, H. Lacker, S. Monteil, V. Niess, and S. T’Jampens. Anatomy of New Physics in $B - \overline{B}$ mixing. *Phys. Rev.*, D83:036004, 2011, 1008.1593.
- [62] Alexander Lenz and Ulrich Nierste. Numerical Updates of Lifetimes and Mixing Parameters of B Mesons. In *CKM unitarity triangle. Proceedings, 6th International Workshop, CKM 2010, Warwick, UK, September 6-10, 2010*, 2011, 1102.4274.
- [63] U. Nierste. Private communication.
- [64] S. Aoki et al. FLAG Review 2019. *Eur. Phys. J.*, C80(2):113, 2020, 1902.08191.
- [65] R. J. Dowdall, C. T. H. Davies, R. R. Horgan, G. P. Lepage, C. J. Monahan, J. Shigemitsu, and M. Wingate. Neutral B-meson mixing from full lattice QCD at the physical point. *Phys. Rev.*, D100(9):094508, 2019, 1907.01025.
- [66] P. A. Zyla et al. Review of Particle Physics. *PTEP*, 2020(8):083C01, 2020.
- [67] Y. Aoki et al. FLAG Review 2021. 11 2021, 2111.09849.
- [68] Albert M Sirunyan et al. Measurements of the Higgs boson width and anomalous HVV couplings from on-shell and off-shell production in the four-lepton final state. *Phys. Rev.*, D99(11):112003, 2019, 1901.00174.

- [69] Philip Bechtle, Oliver Brein, Sven Heinemeyer, Georg Weiglein, and Karina E. Williams. HiggsBounds: Confronting Arbitrary Higgs Sectors with Exclusion Bounds from LEP and the Tevatron. *Comput. Phys. Commun.*, 181:138–167, 2010, 0811.4169.
- [70] Philip Bechtle, Oliver Brein, Sven Heinemeyer, Georg Weiglein, and Karina E. Williams. HiggsBounds 2.0.0: Confronting Neutral and Charged Higgs Sector Predictions with Exclusion Bounds from LEP and the Tevatron. *Comput. Phys. Commun.*, 182:2605–2631, 2011, 1102.1898.
- [71] Philip Bechtle, Oliver Brein, Sven Heinemeyer, Oscar Stal, Tim Stefaniak, Georg Weiglein, and Karina Williams. Recent Developments in HiggsBounds and a Preview of HiggsSignals. *PoS, CHARGED2012:024*, 2012, 1301.2345.
- [72] Philip Bechtle, Oliver Brein, Sven Heinemeyer, Oscar Stål, Tim Stefaniak, Georg Weiglein, and Karina E. Williams. HiggsBounds – 4: Improved Tests of Extended Higgs Sectors against Exclusion Bounds from LEP, the Tevatron and the LHC. *Eur. Phys. J.*, C74(3):2693, 2014, 1311.0055.
- [73] Philip Bechtle, Sven Heinemeyer, Oscar Stal, Tim Stefaniak, and Georg Weiglein. Applying Exclusion Likelihoods from LHC Searches to Extended Higgs Sectors. *Eur. Phys. J.*, C75(9):421, 2015, 1507.06706.
- [74] <https://higgsbounds.hepforge.org/>.
- [75] Philip Bechtle, Daniel Dercks, Sven Heinemeyer, Tobias Klingl, Tim Stefaniak, Georg Weiglein, and Jonas Wittbrodt. HiggsBounds-5: Testing Higgs Sectors in the LHC 13 TeV Era. *Eur. Phys. J.*, C80(12):1211, 2020, 2006.06007.
- [76] Oscar Stål and Tim Stefaniak. Constraining extended Higgs sectors with HiggsSignals. *PoS, EPS-HEP2013:314*, 2013, 1310.4039.
- [77] Philip Bechtle, Sven Heinemeyer, Oscar Stål, Tim Stefaniak, and Georg Weiglein. HiggsSignals: Confronting arbitrary Higgs sectors with measurements at the Tevatron and the LHC. *Eur. Phys. J.*, C74(2):2711, 2014, 1305.1933.
- [78] Philip Bechtle, Sven Heinemeyer, Oscar Stål, Tim Stefaniak, and Georg Weiglein. Probing the Standard Model with Higgs signal rates from the Tevatron, the LHC and a future ILC. *JHEP*, 11:039, 2014, 1403.1582.
- [79] Philip Bechtle, Sven Heinemeyer, Tobias Klingl, Tim Stefaniak, Georg Weiglein, and Jonas Wittbrodt. HiggsSignals-2: Probing new physics with precision Higgs measurements in the LHC 13 TeV era. *Eur. Phys. J.*, C81(2):145, 2021, 2012.09197.
- [80] Johan Alwall, Michel Herquet, Fabio Maltoni, Olivier Mattelaer, and Tim Stelzer. MadGraph 5 : Going Beyond. *JHEP*, 06:128, 2011, 1106.0522.
- [81] https://github.com/LHC-DMWG/model-repository/tree/master/models/Pseudoscalar_2HDM.
- [82] <https://www.hepdata.net/record/ins1782373>.
- [83] <https://atlas.web.cern.ch/Atlas/GROUPS/PHYSICS/PAPERS/EXOT-2018-43/#auxstuff>.

- [84] Mihailo Backovic, Michael Krämer, Fabio Maltoni, Antony Martini, Kentarou Mawatari, and Mathieu Pellen. Higher-order QCD predictions for dark matter production at the LHC in simplified models with s-channel mediators. *Eur. Phys. J.*, C75(10):482, 2015, 1508.05327.
- [85] <https://www.hepdata.net/record/ins1633591>.
- [86] Armen Tumasyan et al. Search for new particles in events with energetic jets and large missing transverse momentum in proton-proton collisions at $\sqrt{s} = 13$ TeV. *JHEP*, 11:153, 2021, 2107.13021.
- [87] <https://www.hepdata.net/record/ins1894408>.
- [88] Mihailo Backovic, Kyoungchul Kong, and Mathew McCaskey. MadDM v.1.0: Computation of Dark Matter Relic Abundance Using MadGraph5. *Physics of the Dark Universe*, 5-6:18–28, 2014, 1308.4955.
- [89] Mihailo Backović, Antony Martini, Olivier Mattelaer, Kyoungchul Kong, and Gopolang Mohlabeng. Direct Detection of Dark Matter with MadDM v.2.0. *Phys. Dark Univ.*, 9-10:37–50, 2015, 1505.04190.
- [90] Federico Ambrogio, Chiara Arina, Mihailo Backovic, Jan Heisig, Fabio Maltoni, Luca Mantani, Olivier Mattelaer, and Gopolang Mohlabeng. MadDM v.3.0: a Comprehensive Tool for Dark Matter Studies. *Phys. Dark Univ.*, 24:100249, 2019, 1804.00044.
- [91] Giorgio Arcadi, Manfred Lindner, Farinaldo S. Queiroz, Werner Rodejohann, and Stefan Vogl. Pseudoscalar Mediators: A WIMP model at the Neutrino Floor. *JCAP*, 1803:042, 2018, 1711.02110.
- [92] Nicole F. Bell, Giorgio Busoni, and Isaac W. Sanderson. Loop Effects in Direct Detection. *JCAP*, 1808:017, 2018, 1803.01574. [Erratum: JCAP1901,E01(2019)].
- [93] N. Aghanim et al. Planck 2018 results. VI. Cosmological parameters. *Astron. Astrophys.*, 641:A6, 2020, 1807.06209. [Erratum: Astron.Astrophys. 652, C4 (2021)].
- [94] E. Aprile et al. Dark Matter Search Results from a One Ton-Year Exposure of XENON1T. *Phys. Rev. Lett.*, 121(11):111302, 2018, 1805.12562.
- [95] Alexander Belyaev, James Blandford, and Daniel Locke. Phenodata database. <https://hepmdb.soton.ac.uk/phenodata>, Jan. 2017.
- [96] Otto Eberhardt, Ana Peñuelas Martínez, and Antonio Pich. Global fits in the Aligned Two-Higgs-Doublet model. *JHEP*, 05:005, 2021, 2012.09200.
- [97] Tetsuya Enomoto and Ryoutaro Watanabe. Flavor constraints on the Two Higgs Doublet Models of Z_2 symmetric and aligned types. *JHEP*, 05:002, 2016, 1511.05066.
- [98] Albert M Sirunyan et al. Combined measurements of Higgs boson couplings in proton–proton collisions at $\sqrt{s} = 13$ TeV. *Eur. Phys. J.*, C79(5):421, 2019, 1809.10733.
- [99] Georges Aad et al. Combined measurements of Higgs boson production and decay using up to 80 fb^{-1} of proton-proton collision data at $\sqrt{s} = 13$ TeV collected with the ATLAS experiment. *Phys. Rev.*, D101(1):012002, 2020, 1909.02845.

- [100] Felix Kling, Shufang Su, and Wei Su. 2HDM Neutral Scalars under the LHC. *JHEP*, 06:163, 2020, 2004.04172.
- [101] Tao Han, Shuailong Li, Shufang Su, Wei Su, and Yongcheng Wu. Comparative Studies of 2HDMs under the Higgs Boson Precision Measurements. *JHEP*, 01:045, 2021, 2008.05492.
- [102] A combination of measurements of Higgs boson production and decay using up to 139 fb^{-1} of proton–proton collision data at $\sqrt{s} = 13 \text{ TeV}$ collected with the ATLAS experiment. Technical Report ATLAS-CONF-2020-027, CERN, Geneva, Aug 2020.
- [103] Georges Aad et al. Search for heavy Higgs bosons decaying into two tau leptons with the ATLAS detector using pp collisions at $\sqrt{s} = 13 \text{ TeV}$. *Phys. Rev. Lett.*, 125(5):051801, 2020, 2002.12223.
- [104] Morad Aaboud et al. Search for pair production of Higgs bosons in the $b\bar{b}b\bar{b}$ final state using proton-proton collisions at $\sqrt{s} = 13 \text{ TeV}$ with the ATLAS detector. *JHEP*, 01:030, 2019, 1804.06174.
- [105] Morad Aaboud et al. Search for a heavy Higgs boson decaying into a Z boson and another heavy Higgs boson in the $\ell\bar{\ell}b\bar{b}$ final state in pp collisions at $\sqrt{s} = 13 \text{ TeV}$ with the ATLAS detector. *Phys. Lett.*, B783:392–414, 2018, 1804.01126.
- [106] Search for heavy resonances decaying into a Z boson and a Higgs boson in final states with leptons and b -jets in 139 fb^{-1} of pp collisions at $\sqrt{s} = 13 \text{ TeV}$ with the ATLAS detector. Technical report, CERN, Geneva, Aug 2020. All figures including auxiliary figures are available at <https://atlas.web.cern.ch/Atlas/GROUPS/PHYSICS/CONFNOTES/ATLAS-CONF-2020-043>.
- [107] Serguei Chatrchyan et al. Measurement of the Properties of a Higgs Boson in the Four-Lepton Final State. *Phys. Rev.*, D89(9):092007, 2014, 1312.5353.
- [108] Georges Aad et al. Search for a heavy Higgs boson decaying into a Z boson and another heavy Higgs boson in the $\ell\bar{\ell}b\bar{b}$ and $\ell\bar{\ell}WW$ final states in pp collisions at $\sqrt{s} = 13 \text{ TeV}$ with the ATLAS detector. *Eur. Phys. J.*, C81(5):396, 2021, 2011.05639.
- [109] Jan Kalinowski, Wojciech Kotlarski, Tania Robens, Dorota Sokolowska, and Aleksander Filip Zarnecki. Exploring Inert Scalars at CLIC. *JHEP*, 07:053, 2019, 1811.06952.
- [110] J. de Blas et al. The CLIC Potential for New Physics. 3/2018, 12 2018, 1812.02093.
- [111] B. Abi et al. Measurement of the Positive Muon Anomalous Magnetic Moment to 0.46 ppm. *Phys. Rev. Lett.*, 126:141801, 2021, 2104.03281.
- [112] Adriano Cherchiglia, Dominik Stoeckinger, and Hyejung Stoeckinger-Kim. Muon $g-2$ in the 2HDM: maximum results and detailed phenomenology. *Phys. Rev.*, D98:035001, 2018, 1711.11567.
- [113] P. M. Ferreira, B. L. Gonçalves, F. R. Joaquim, and Marc Sher. $(g-2)\mu$ in the 2HDM and slightly beyond: An updated view. *Phys. Rev. D*, 104(5):053008, 2021, 2104.03367.
- [114] Adriano Cherchiglia, Patrick Kneschke, Dominik Stöckinger, and Hyejung Stöckinger-Kim. The muon magnetic moment in the 2HDM: complete two-loop result. *JHEP*, 01:007, 2017,

1607.06292. [Erratum: JHEP 10, 242 (2021)].

- [115] G. W. Bennett et al. Final Report of the Muon E821 Anomalous Magnetic Moment Measurement at BNL. *Phys. Rev.*, D73:072003, 2006, hep-ex/0602035.